International Journal of Control, Automation, and Systems VV(X) (YYYY) 1-16
http://dx.doi.org/10.1007/s12555-xxx-xxxx-x
ISSN:1598-6446 eISSN:2005-4092
http://www.springer.com/12555

Fault Tolerant Flight Control for the Traction Phase of Pumping Airborne Wind Energy Systems

Tareg Mohammed , Espen Oland , and Lorenzo Fagiano*

Abstract: A fault-tolerant control approach is proposed, for a pumping Airborne Wind Energy System (AWES) comprising a tethered fixed-wing aircraft with integrated propellers for vertical take-off and landing (VTOL). First, the flight control design for the traction phase of the system, when the tethered aircraft has to fly in loops using the rudder, is presented. Then, the presence of the propellers, that are normally not used in the traction phase, is exploited to obtain a fault tolerant controller in case of rudder malfunctioning. The approach detects a possible discrete control surface fault and compensates for the loss in actuation by using the VTOL system. A sophisticated model of the system is used to analyse the performance of the proposed technique. The main finding is that the approach is able to handle abrupt rudder faults with high tolerance.

Keywords: Airborne Wind Energy, Fault-tolerant Control, High-altitude wind, Flight control, Nonlinear control

1. INTRODUCTION

Airborne Wind Energy Systems (AWES) employ an autonomous tethered aircraft to convert wind energy into electricity. AWES have the potential to offer economically viable and sustainable electricity production on a large scale, according to many studies such as [1, 2, 4, 7, 10, 22]. These studies consider the advantages of AWES in terms of low capital costs and easy installation, and their capability to reach wind above 300m above ground. A key assumption is that the system is highly robust and able to operate reliably for long periods of time. To this end, much research and development still need to be addressed in terms of operational safety, fault-handling, and reconfiguration strategies ([12]). As stated by the study [17], most failure mitigation measures in AWE can be obtained by fault detection and isolation and corresponding recovery actions. Notwithstanding the many problems of interest, the scientific literature on these aspects is rather limited. The variety of AWE concepts ([8, 12, 21]) makes it unfeasible to develop general fault-tolerant techniques that work properly for all of them. Rather, specific fault-tolerant approaches shall be developed for each system/subsystem and each relevant operating phase. Regarding the aircraft, redundancy of sensors and control units can be employed to increase resilience and implement recovery actions, while actuator redundancy is more difficult to apply, due to the need to keep the airborne mass low. [3] presents an electrical layout and control strategy to achieve fault tolerance for AWES with onboard generators (the so-called drag power approach, different from the pumping approach considered here). In [9], modeling and control aspects and post-fault operation of the electric drives are considered. In [14], we presented an approach to fault-tolerant control of a tethered aircraft flying in circles parallel to the ground, with low tether force.

In this work, we consider the same AWES class as [14], i.e., with pumping operation, rigid aircraft, and vertical take-off and landing (VTOL). Pumping AWES accomplish periodic cycles of traction and retraction phases, linked by suitable transitions, see e.g. [19]. In these cycles, the aircraft operates in dynamic flight mode, controlled by means of discrete control surfaces similar to those of a glider, and the tether force can be either very large (in the traction phase) or very low (during retraction and transitions). The operation starts and finishes with VTOL phases, carried out with onboard propellers in a very different flight mode, similar to a tethered multicopter. Besides the small ground area required for take-off and landing [11], an advantage of the VTOL system is that it provides redundancy of control actuators, allowing us to design effective recovery actions in case of actuator faults.

This research has been supported by Fondazione Cariplo under grant n. 2022-2005, project “NextWind - Advanced control solutions for large scale Airborne Wind Energy Systems”, by the European Union–Next Generation EU in the context of the project PNRR M4C2, Investimento 1.3 DD. 341 del 15 marzo 2022 – NEST – Network 4 Energy Sustainable Transition – Spoke 2 - PE00000021 - D43C22003090001, and by the Italian Ministry of University and Research under grants “P2022927H7 - DeepAirborne – Advanced Modeling, Control and Design Optimization Methods for Deep Offshore Airborne Wind Energy”.
Tareg Mohammed is with Kitemill AS - Voss, 5704, Norway, and Politecnico di Milano - Dipartimento di Elettronica, Informazione e Bioingegneria - 20133 Milano MI, Italy (e-mail: tareg.mohammed@polimi.it). Espen Oland is with UiT - The Arctic University of Norway - 8514 Narvik, Norway (e-mail: espen.oland@uit.no). Lorenzo Fagiano is with Politecnico di Milano - Dipartimento di Elettronica, Informazione e Bioingegneria - 20133 Milano MI, Italy (e-mail: lorenzo.fagiano@polimi.it).
* Corresponding author.

Building on [14], this paper introduces a new fault-tolerant control approach for the traction phase, when the aircraft is in crosswind flight. As a first contribution, we describe a new design approach of a flight controller for this phase of the pumping cycle, where the rudder is normally used to obtain circular crosswind flight patterns. Then, as a second contribution we present an active fault tolerant control (AFTC) scheme to detect and accommodate a possible rudder failure, providing the required control input with the onboard propellers of the VTOL system. The fault detection approach is based on the difference between the observed angular accelerations and those expected on the basis of the commanded input. When a rudder fault is detected, the rotors are engaged to generate the control moments issued by the flight controller. The latter is not modified, so that the aircraft continues flying its prescribed path until a high-level strategy commands a transition to hovering and then landing. In this way, we reduce the risk of stalling and/or entangling the aircraft with the tether, which would be higher with a more abrupt transition to hovering. We test the approach on a high-fidelity model of the system, showing that it effectively and reliably manages to accommodate faults in a wide range of wind conditions.
The paper is organized as follows: Section 2 describes the system and its model. Section 3 describes the proposed fault-tolerant control design, including the nominal controller, the active fault tolerant control (AFTC) approach, and the control allocation technique for the four propellers. Section 4 presents the results obtained by applying our approach on a detailed simulator, and conclusions are drawn in Section 5.

1.1. Notation and list of symbols

Bold-faced symbols denote three-dimensional vectors. The same symbol non-bold and with an added subscript denotes the component of that vector along the direction named after the subscript (e.g., $F_{t,x}$ is the component of vector $\boldsymbol{F}_t$ in the body x-direction). A list of symbols employed in the paper follows.

Symbol	Description
A	Wind reference frame
A_p	Propeller swap area
B	Traction reference frame
$\hat{B}_Q$	Quad rotor control allocation matrix
$\hat{B}_S$	Dynamic control effectiveness matrix
C_{D}	Aerodynamic drag coefficient
C_{L}	Aerodynamic lift coefficient
C_{l}	Aerodynamic roll coefficient
C_{m}	Aerodynamic pitch coefficient
C_{n}	Aerodynamic yaw coefficient
C_{Y}	Aerodynamic side force coefficient
CG	Aircraft center of gravity
$\boldsymbol{F}_A$	Aerodynamic force vector
F_D	Aerodynamic drag force
F_L	Aerodynamic lift force
F_{P_z}	Sum of propellers' thrust along the aircraft z-axis
F_{ref}	Desired tether pulling force
$\boldsymbol{F}_t$	Tether force exerted on the aircraft
$\overline{F}_t$	Tether breaking load
$\boldsymbol{F}_{t_{GS}}$	Tether force exerted on the winch
$F_{T_{z,d}}$	Desired thrust along aircraft z-axis
F_Y	Aerodynamic side force
$\bar{J}_P$	Inertia matrix of the propeller
J_P	Propeller inertia about its axis
J_{xx}	Aircraft moment of inertia about the x-axis
J_{xz}	Cross-moment of inertia about the x- and z-axis
J_{yy}	Aircraft moment of inertia about the y-axis
J_{zz}	Aircraft moment of inertia about the z-axis
K_c	Circular path error correction gain
K_d	Rotor spinning speed decreasing gain for saturation management
K_r	Yaw rate controller gain
K_t	Total tether stiffness
$K_{t,e}$	Tether stiffness per segment
K_u	Rotor spinning speed increasing gain for saturation management
K_{winch}	Winch controller feedback gains
K_υ	Reference yaw rate controller gain
(L,M,N)	Axes of the traction reference frame
$\boldsymbol{M}_{G,i}$	i^{th} propeller gyroscopic moment
$\boldsymbol{M}_{G,tot}$	Vector sum of $\boldsymbol{M}_{G,i}$ over $i=1,\dots,4$
$\boldsymbol{M}_A$	Aerodynamic moment
$\boldsymbol{M}_d$	Desired aircraft moment
$\boldsymbol{M}_t$	Moment exerted by the tether on aircraft
N_t	Number of nodes in the tether model
$\boldsymbol{O}_B$	Vector pointing from the origin of wind frame to the origin of the traction frame
$P_{induced,i}$	i^{th} propeller induced power
$P_{profile,i}$	i^{th} propeller profile power
$Q_{i,max}$	i^{th} propeller maximum torque
Q_{P_i}	i^{th} propeller aerodynamic torque
R_{2-norm}	2-norm of the residuals R_x,R_y, and R_z
R_p	Propeller blade total length
R_t	Desired helical path radius
R_x	Aircraft roll moment residual
R_y	Aircraft pitch moment residual
R_z	Aircraft yaw moment residual
S	Wing surface area
T_i	i^{th} propeller thrust
$T_{i,max}$	i^{th} propeller maximum delivered thrust
U	Aircraft speed along the body x-axis
V	Aircraft speed along the body y-axis

W	Aircraft speed along the body z-axis
$\boldsymbol{W}_s$	Absolute wind speed vector
(X,Y,Z)	Axes of the wind reference frame
a_p	Propeller blade lift curve
b	Wing span
b_i	i^{th} motor thrust to squared speed ratio
b_p	Number of blades of each propeller
$\bar{c}$	Wing cord
c_i	i^{th} motor torque to squared speed ratio
c_p	Propeller blade effective cord
d	Distance between the aircraft position projected on the (L,M)-plane and the origin of the traction frame
h	Aircraft altitude from ground level
h_{min}	Minimum allowable aircraft height
ℓ_t	Tether length
$\ell_{t,min}$	Minimum allowable tether length
m_a	Mass of the aircraft
p	Aircraft angular rate about the x-axis
$\hat{\dot{p}}$	Estimated angular acceleration about the x-axis
$\boldsymbol{p}_k$	Aircraft position vector
$\boldsymbol{p}_{O_B}^B$	Aircraft position relative to the origin of the traction frame, expressed in the traction frame
$\dot{\boldsymbol{p}}_k{}^B$	Aircraft velocity vector expressed in the traction frame
$\boldsymbol{p}_{P_i/CG}$	Location of propeller i with respect to CG
q	Aircraft angular rate about the y-axis
$\hat{q}$	Aircraft attitude quaternion
$\hat{\dot{q}}$	Estimated angular acceleration about the y-axis
$\hat{q}_{B/A}$	Quaternion rotation from the wind frame to the traction frame
q_∞	Dynamic pressure
r	Aircraft angular rate about the z-axis
$\hat{\dot{r}}$	Estimated angular acceleration about the z-axis
r_{ref}	Reference yaw rate in traction frame
$\boldsymbol{v}_a$	Apparent wind vector at the aircraft
v_i	i^{th} propeller induced velocity
v_i'	i^{th} propeller effective flow speed
$\boldsymbol{v}_{P_i}$	i^{th} propeller blades' velocity vector relative to air
v_t	Tether linear reel-out speed
v_t^{ref}	Tether reference linear reel-out speed
x_p	x-axis distance of front/aft motors from CG
y_p	y-axis position of left/right motors from CG
α	Aircraft angle of attack
β	Aircraft side slip angle
δ_a	Aircraft aileron deflection
δ_e	Aircraft elevator deflection
δ_r	Aircraft rudder deflection
$\overline{\varepsilon}_t$	Tether elongation at tether breaking load
θ_0	Propeller blade angle in the root of the hub
θ_1	Propeller blade linear twist
θ_h	Elevation angle of traction phase of helical path axis from ground surface
$\rho(h)$	Air density at altitude h
τ_w	Time constant of winch speed control loop
υ	Velocity angle of the aircraft projected in the (L,M)-plane
χ^c	Desired flying course in traction frame
$\tilde{\omega}_{b/A}$	Skew-symmetric matrix of the aircraft angular velocity relative to the inertial frame
Ω_i	i^{th} propeller spinning speed
$\Omega_{M,max}$	Maximum spinning speed achievable by the motor
$\Omega_{M,min}$	Minimum spinning speed set to the motor
$\boldsymbol{\omega}_{P,i}$	i^{th} Propeller angular velocity vector

2. SYSTEM DESCRIPTION AND MODELING

The AWES under consideration is illustrated in fig. 1, which shows its layout, main subsystems, and power generation operating principle. The system consists of a ground station connected to the aircraft through a tether

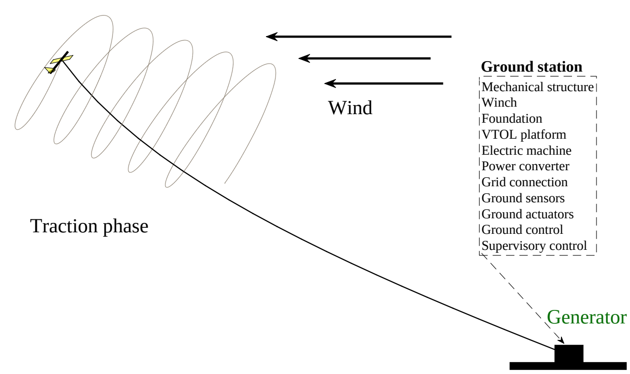

(a) Traction phase (power generation)

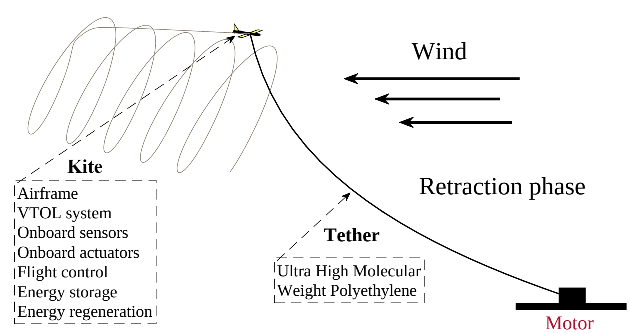

(b) Retraction phase (power consumption)

Fig. 1. Main subsystems and components of the Airborne Wind Energy System (AWES) considered in this paper, with a rigid wing and Vertical Take-Off and Landing (VTOL) system. The figure also presents the two main phases of power generation, namely traction and retraction. The focus of this work is the flight control system during the traction phase.

made of polymeric material. The ground station features an electric machine that can act as either a generator or a motor, depending on the operational phase, connected to a winch with a spooling system, which can reel in or out the tether. The aircraft has a rigid wing with discrete control surfaces and four vertical-axis propellers, as shown in fig. 2, which is a real-world, small-scale system developed by Kitemill. In the so-called traction phase (see Fig. 1), the aircraft flies fast in crosswind conditions: the generated lift force is large enough to keep the aircraft airborne and to apply a large force on the tether. The latter is reeled out until a prescribed maximum value, while the electric machine on ground applies an opposite torque, thus generating energy. In the retraction phase, a small fraction of such energy is consumed to reel-in the tether under low force with the electric machine, while the aircraft glides towards the ground station until a pre-defined minimum tether length is reached, and a new cycle starts. The resulting pumping cycle achieves a net positive average power that depends on the wind speed. We refer the reader to [12] and the references therein for more details on the fundamentals and state of the art of airborne wind energy systems.

In the remainder, we consider a body reference system (x,y,z), fixed to the aircraft. The x-axis points forward along the fuselage, the z-axis points downward, and the y-axis completes the right-handed system. We also consider an inertial, right-handed reference system $A = (X,Y,Z)$, named the wind frame, with the X-axis pointing in the prevailing wind direction, and Z-axis normal to the ground and pointing downwards along the Earth's gravity. The origin of frame A is located at the ground station, and the aircraft position is given by vector $\boldsymbol{p}_k$. We denote with $h = -p_{k,Z}$ the aircraft's height above ground. In the remainder, we omit the continuous time variable $t \in \mathbb{R}$ for the sake of simplicity; constant parameters can be distinguished from time-dependent variables based on the context.

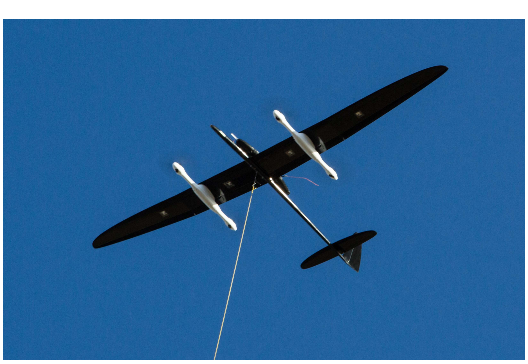

Fig. 2. The small-scale “KM0” aircraft developed by the company Kitemill.

2.1. Winch and tether models

The winch is modeled in close loop with a velocity-tracking controller, expressed in the Laplace domain as:

$$v_t(s) = \frac{1}{\tau_w s + 1} v_t^{ref}(s),$$

where s is the Laplace variable, v_t is the linear reel-out speed of the tether, v_t^{ref} its reference value, and τ_w is the close-loop time constant. Such an approximation is suitable for this study, which is focused on the flight control system. The value of v_t^{ref} is computed by a higher-level controller, as described in Section 3.
The tether model is described in detail in [5, 6, 13], and briefly recalled here for completeness. It features a series of lumped masses at N_t nodes. Considering the three-dimensional (3D) position and velocity of each node, the state of the tether model has thus dimensions $6N_t$. Considering the N_t nodes plus the ground station and aircraft at the two extremes, there are $N_t + 1$ segments in total. Any such segment is modeled as a linear damper in parallel with a nonlinear spring, where the nonlinearity accounts for the fact that the tether can transfer forces only when taut. Moreover, the aerodynamic drag forces acting on each tether segment are considered. The balance of forces on each node determines the corresponding 3D acceleration vector, which is integrated twice to obtain velocity and position vectors. The length of reeled-out tether, denoted by ℓ_t, is computed by integrating the winch speed:

$$\dot{\ell}_t = v_t.$$

The total tether stiffness is determined by:

$$K_t = \frac{\overline{F}_t}{\overline{\varepsilon}_t \ell_t}$$

where $\overline{F}_t$ and $\overline{\varepsilon}_t$ denote the tether breaking load and corresponding elongation, respectively. For instance, $\overline{\varepsilon}_t = 0.03$ means that the breaking load corresponds to 3% of elongation. Since the tether elements are in series, the stiffness $K_{t,e}$ of each one is computed as:

$$K_{t,e} = (N_t + 1)K_t.$$

which preserves the overall stiffness. Thus, the stiffness of each tether element is not constant, rather it depends on the winch position via the tether length. The other tether parameters (viscous friction coefficient, mass per unit of length, diameter, drag coefficient) are assumed constant. To link the tether model to those of the other subsystems, the motion of the ground extreme is imposed equal to zero, and that of the aircraft side equal to the aircraft's 3D position and velocity. The forces applied at the tether extremes corresponding to the winch and to the aircraft are denoted, respectively, with $\boldsymbol{F}_{t_{GS}}$ and $\boldsymbol{F}_t$. The tether is assumed to be attached at the aircraft's center of gravity CG, and therefore it does not exert any moment on the aircraft body.

2.2. Propellers' thrust and torque models

The rotors are 2-bladed propellers, each producing thrust without the capability of inverse rotation. In untethered multicopter modeling, the effect of apparent airspeed on the propellers' flow, thrust, and torque is often overlooked due to the relatively small apparent wind velocity experienced by the aerial vehicle. However, the AWES considered here operates at a minimum of fourteen meters per second apparent wind speed during looping, necessitating improved modeling of this aspect. Therefore, we created a detailed lookup table that considers several variables that affect the propellers' functioning. Let us denote the apparent velocity vector of the aircraft with $\boldsymbol{v}_a$:

$$\boldsymbol{v}_a = \begin{bmatrix} v_{a,x} \\ v_{a,y} \\ v_{a,z} \end{bmatrix} = \begin{bmatrix} W_{s,x}(\boldsymbol{p}_k) - U \\ W_{s,y}(\boldsymbol{p}_k) - V \\ W_{s,z}(\boldsymbol{p}_k) - W \end{bmatrix}$$

Here $\boldsymbol{W}_s$ is the absolute wind speed vector, expressed in the body frame, at the aircraft position $\boldsymbol{p}_k$, and U, V, and W are the aircraft's velocity vector components relative to the ground and expressed in the body frame. The first step is to calculate, for each rotor $i = 1,2,3,4$, the velocity vector relative to air at the propeller's blades, which is denoted by $\boldsymbol{v}_{P_i}$ and can be obtained using the following equation:

$$\boldsymbol{v}_{P_i} = \begin{bmatrix} v_{P_i,x} \\ v_{P_i,y} \\ v_{P_i,z} \end{bmatrix} = \boldsymbol{v}_a + \tilde{\omega}_{b/A}\, \boldsymbol{p}_{P_i/CG} \tag{1}$$

In equation (1), $\boldsymbol{p}_{P_i/CG}$ denotes the location of propeller i with respect to CG, while $\tilde{\omega}_{b/A}$ is a skew-symmetric matrix indicating the aircraft angular velocity relative to the inertial frame A.

The effective flow speed, denoted by v'_i, is then calculated as follows:

$$v'_i = \sqrt{{v_{P_i,x}}^2 + {v_{P_i,y}}^2 + (v_{P_i,z} - v_i)^2} \tag{2}$$

Here, v_i represents the induced velocity of the propeller under consideration, to be determined. The thrust of the propeller is a function of both v'_i and v_i and is given by:

$$T_i = 2\rho(h) A_p v'_i v_i \tag{3}$$

In this equation, $\rho(h)$ is the air density as a function of altitude h, $A_p = \pi R_p^2$, and R_p is the propeller's diameter. Additionally, the thrust T_i can also be expressed using the following equation, which depends on the airspeed components and propeller's parameters ([18]):

$$\begin{aligned} T_i \quad = \quad & \frac{\rho(h) a_p b_p c_p R_p}{4} \left[(v_{P_i,z} - v_i)\, \Omega_i R_p + \right. \\ & \tfrac{2}{3} (\Omega_i R_p)^2 \left(\theta_0 + \tfrac{3}{4}\theta_1\right) + \\ & \left. \left({v_{P_i,x}}^2 + {v_{P_i,y}}^2\right) \left(\theta_0 + \tfrac{1}{2}\theta_1\right) \right] \end{aligned} \tag{4}$$

In this equation, Ω_i represents the propeller's rotational speed, b_p is the number of blades, c_p is the blade's effective chord, θ_0 is the root blade angle, θ_1 is the linear twist along the blade, and a_p is the slope of the blade's airfoil lift curve.

Solving numerically equations (2), (3) and (4), we obtain lookup tables for thrust T_i and induced velocity v_i for each propeller. Each lookup table has five inputs, i.e., $v_{P_i,x}, v_{P_i,y}, v_{P_i,z}, \Omega_i, h$. An interpolation algorithm is then utilized to determine each propeller's thrust and induced velocity for a given operational condition. These lookup tables are referred to as:

$$T_i = f_T(v_{P_i,x}, v_{P_i,y}, v_{P_i,z}, \Omega_i, h)$$

$$v_i = f_v(v_{P_i,x}, v_{P_i,y}, v_{P_i,z}, \Omega_i, h)$$

As an example, Figs. 3(a)-3(b) show the propeller thrust as a function of the apparent wind components, and Fig. 4 shows the rotors' induced velocity at different operating conditions. It can be seen how the apparent velocity's vertical component strongly affects the propeller's thrust and induced velocity.

To calculate the aerodynamic torque of each rotor/propeller, denoted with Q_{P_i}, we use a formula that takes into account the thrust, surrounding airspeed, and rotor spinning speed:

$$P_{induced,i} = T_i\,(v_i - v_{P_i,z})$$

$$P_{profile,i} = \frac{\rho\, C_{d_0} b_p c_p\, \Omega_i R_p^2}{8} \left[(\Omega_i R_p)^2 + {v_{P_i,x}}^2 + {v_{P_i,y}}^2 \right]$$

$$Q_{P_i} = \frac{1}{\Omega_i} \left(P_{induced,i} + P_{profile,i}\right) \tag{5}$$

The induced power and profile power denoted as $P_{induced,i}$ and $P_{profile,i}$, respectively.where the zero-lift drag coefficient of the propeller blade's airfoil is represented by C_{d_0}, see [18] for details. We also include the gyroscopic moment exerted by each motor/propeller on the aircraft, denoted with $\boldsymbol{M}_{G,i}$:

$$\boldsymbol{M}_{G,i} = -\,\tilde{\omega}_{b/A}\, \bar{J}_P\, \boldsymbol{\omega}_{P,i} \tag{6}$$

where $\bar{J}_P$ is the inertia matrix for the propeller, and $\boldsymbol{\omega}_{P,i}$ is the angular velocity vector of the spinning rotor. For a propeller/rotor with rotational axis aligned with the positive body z-axis and moment of inertia J_P, equation (6) can be simplified as follows:

$$\boldsymbol{M}_{G,i} = -\,\tilde{\omega}_{b/A} \begin{bmatrix} 0 \\ 0 \\ J_P \Omega_i \end{bmatrix} \tag{7}$$

We finally denote with $M_{G,x}$ $M_{G,y}$ $M_{G,z}$ the algebraic sum over $i = 1, \ldots, 4$ of the x, y, z components of $\boldsymbol{M}_{G,i}$.

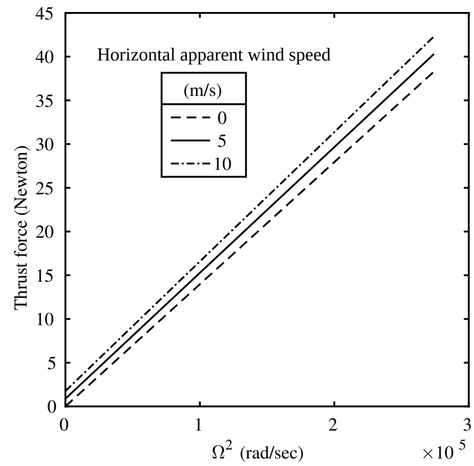

(a) $h = 0, v_{P,y} = v_{P,z} = 0$

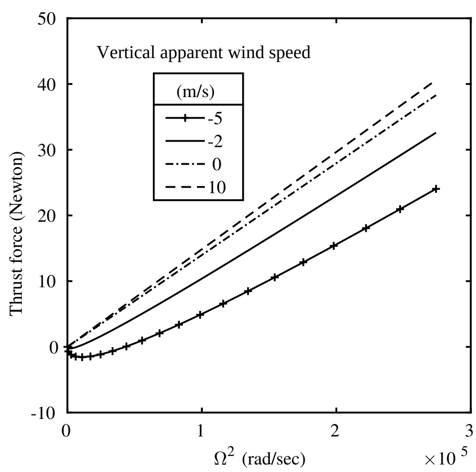

(b) $h = 0, v_{P,x} = v_{P,y} = 0$

Fig. 3. Propeller thrust as a function of the propeller speed, for various horizontal (a) or vertical (b) apparent speed values.

2.3. Aircraft model

To derive the state-space ordinary differential equations for the aircraft model, we consider the forces and moments generated by the aerodynamics, propellers, tether, and gravity. The aircraft angle of attack α and sideslip angle β are derived using the following equations:

$$\alpha = \text{atan2}(v_{a,z}, v_{a,x})$$

$$\beta = \arcsin(v_{a,y}/v_a)$$

The aircraft apparent airspeed is $v_a = \|\boldsymbol{v}_a\|_2$. To calculate the total drag, side force, and lift aerodynamic coefficients

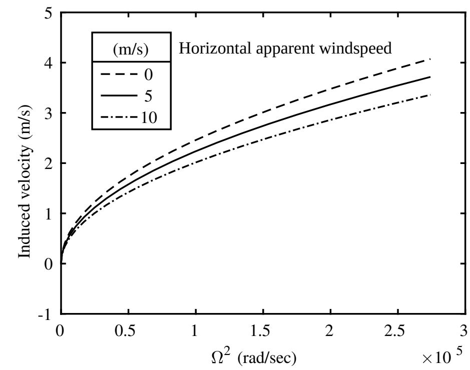

(a) v_i at $h = 0, v_{P,y} = v_{P,z} = 0$

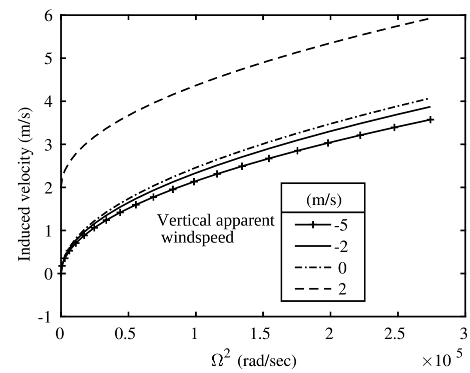

(b) v_i at $h = 0, v_{P,x} = v_{P,y} = 0$

Fig. 4. Induced velocity as a function of the propeller speed, for various horizontal (a) or vertical (b) apparent speed values.

($C_{\mathrm{D}}, C_{\mathrm{Y}}$, and C_{L}, respectively), equation (8) is utilized:

$$\begin{aligned} C_{\mathrm{D}} &= C_{\mathrm{D}}(\alpha) \\ C_{\mathrm{Y}} &= C_{\mathrm{Y}}(\beta, \delta_r) + C_{\mathrm{Y_p}} \frac{pb}{2v_a} + C_{\mathrm{Y_r}} \frac{rb}{2v_a} \\ C_{\mathrm{L}} &= C_{\mathrm{L}}(\alpha, \delta_e) + C_{\mathrm{L_q}} \frac{q\bar{c}}{2v_a} \end{aligned} \tag{8}$$

Where, δ_r and δ_e are the rudder and elevator deflections, respectively, p, q, and r are the aircraft angular velocities about the x, y, and z axis, b is the aircraft wingspan and $\bar{c}$ its mean aerodynamic chord. To compute the total aerodynamic moment coefficient for roll, pitch, and yaw, $C_{\mathrm{l}}, C_{\mathrm{m}}$, and C_{n}, respectively, equation (9) is applied.

$$\begin{aligned} C_{\mathrm{l}} &= C_{\mathrm{l}}(\alpha, \delta_a) + C_{\mathrm{l}}(\beta, \delta_r) + C_{\mathrm{l_p}} \frac{pb}{2v_a} + C_{\mathrm{l_r}} \frac{rb}{2v_a} \\ C_{\mathrm{m}} &= C_{\mathrm{m}}(\alpha, \delta_e) + C_{\mathrm{m_q}} \frac{q\bar{c}}{2v_a} \\ C_{\mathrm{n}} &= C_{\mathrm{n}}(\alpha, \delta_a) + C_{\mathrm{n}}(\beta, \delta_r) + C_{\mathrm{np}} \frac{pb}{2v_a} + C_{\mathrm{nr}} \frac{rb}{2v_a} \end{aligned} \tag{9}$$

Where δ_a is the aileron deflection, and $C_{\mathrm{Y_p}}$, $C_{\mathrm{Y_r}}$, $C_{\mathrm{L_q}}$, $C_{\mathrm{l_p}}$, $C_{\mathrm{l_r}}$, $C_{\mathrm{m_q}}$, $C_{\mathrm{n_p}}$, and $C_{\mathrm{n_r}}$ are the aircraft damping coefficients.

The aerodynamic coefficients and functions appearing in equations (8)-(9) are specific to each aircraft; those used in our simulation study have been sourced from [16] and are omitted here for the sake of brevity. For more information on these coefficients, we refer to this source.
The components of the aircraft's aerodynamic force vector are then calculated as follows:

$$\begin{aligned} F_D &= q_\infty S C_D \\ F_Y &= q_\infty S C_Y \\ F_L &= q_\infty S C_L \end{aligned}$$

where S is the wing area and q_∞ the dynamic pressure, calculated as follow:

$$q_\infty = \frac{1}{2}\rho(h){v_a}^2$$

To obtain the aerodynamic force vector in the aircraft body frame the following rotation is applied:

$$\begin{bmatrix} F_{A_x} \\ F_{A_y} \\ F_{A_z} \end{bmatrix} = \begin{bmatrix} c(\alpha)c(\beta) & -c(\alpha)s(\beta) & -s(\alpha) \\ s(\beta) & c(\beta) & 0 \\ s(\alpha)c(\beta) & -s(\alpha)s(\beta) & c(\alpha) \end{bmatrix} \begin{bmatrix} -F_D \\ F_Y \\ -F_L \end{bmatrix}$$

where $c(\cdot)$ and $s(\cdot)$ stand here for cosine and sine, respectively.
The aerodynamic moments around the axes x, y, z are calculated as:

$$\begin{aligned} M_{A,x} &= q_\infty S b C_l \\ M_{A,y} &= q_\infty S \bar{c} C_m \\ M_{A,z} &= q_\infty S b C_n \end{aligned}$$

and the total vertical thrust contributed by the propellers is:

$$F_{P_z} = -(T_1 + T_2 + T_3 + T_4)$$

where T_i, $i = 1, \ldots, 4$ are the thrust forces contributed by each of the four propellers, see (2)-(4). The propeller moments acting on the body frame x, y and z axis are given by:

$$\begin{aligned} M_{R,x} &= y_p(T_3 + T_2 - T_1 - T_4) \\ M_{R,y} &= x_p(T_1 + T_3 - T_2 - T_4) \\ M_{R,z} &= Q_{P_1} + Q_{P_1} + Q_{P_1} + Q_{P_1} \end{aligned} \tag{10}$$

where x_p, y_p are the distances between the aircraft CG and each rotor along the x-axis and y-axis, respectively (the considered aircraft features a symmetrical configuration; equation (10) can be easily generalized to non-symmetric rotor placements).
Finally, the differential equations of the aircraft model are given by:

$$\dot{U} = \frac{(F_{A_x} + F_{t,x})}{m_a} + g_x - Wq + Vr$$

$$\dot{V} = \frac{(F_{A_y} + F_{t,y})}{m_a} + g_y - Ur + Wp$$

$$\dot{W} = \frac{(F_{A_z} + F_{P_z} + F_{t,z})}{m_a} + g_z - Vp + Uq$$

$$\dot{\hat{q}} = \frac{1}{2} \begin{bmatrix} -q_1 & -q_2 & -q_3 \\ q_0 & -q_3 & q_2 \\ q_3 & q_0 & -q_1 \\ -q_2 & q_1 & q_0 \end{bmatrix} \begin{bmatrix} p \\ q \\ r \end{bmatrix}$$

$$\begin{aligned} \dot{p} &= (c_1 r + c_2 p)q + c_3(M_{A,x} + M_{R,x}) + c_4(M_{A,z} + M_{R,z}) \\ \dot{q} &= c_5 pr - c_6(p^2 - r^2) + c_7(M_{A,y} + M_{R,y}) \\ \dot{r} &= (c_8 p + c_2 r)q + c_4(M_{A,x} + M_{R,x}) + c_9(M_{A,z} + M_{R,z}) \end{aligned}$$

where m_a is the aircraft mass, $\hat{q} = [q_0, q_1, q_2, q_3]^T$ is the quaternion defining the relative orientation of the body frame with respect to the inertial one, g_x, g_y, and g_z are the gravity acceleration components acting in the body frame, computed as $g_x = 2g(q_1 q_3 - q_0 q_2)$; $g_y = 2g(q_2 q_3 - q_0 q_1)$; $g_z = g(q_0^2 - q_1^2 - q_2^2 + q_3^2)$, $\dot{p}, \dot{q}, \dot{r}$ are the angular accelerations about the x, y, z axes. The parameters $c_1, c_2, c_3, c_4, c_5, c_6, c_7, c_8$ and c_9 used in the rotational dynamics' equations are given below:

$$c_1 = \frac{(J_{yy} - J_{zz})J_{zz} - J_{xz}^2}{\Gamma}, \quad c_2 = \frac{(J_{xx} - Jyy + J_{zz})J_{xz}}{\Gamma}$$

$$c_3 = \frac{J_{zz}}{\Gamma}, \quad c_4 = \frac{J_{xz}}{\Gamma}, \quad c_5 = \frac{J_{zz} - J_{xx}}{J_{yy}}, \quad c_6 = \frac{J_{xz}}{J_{yy}}$$

$$c_7 = \frac{1}{J_{yy}}, \quad c_8 = \frac{J_{xx}(J_{xx} - J_{yy}) + J_{xz}^2}{\Gamma}, \quad c_9 = \frac{J_{xx}}{\Gamma}$$

Where $\Gamma = J_{xx}J_{zz} - J_{xz}^2$ and J_{xx}, J_{yy}, J_{zz}, J_{xz} are the non-zero elements of the model inertia matrix.

3. FAULT-TOLERANT FLIGHT CONTROL DESIGN

3.1. Nominal controller

The objective of the control system for the traction phase is to reel-out the tether under a desired pulling force F_{ref}, while the aircraft flies a helical pattern with a constant radius. Fig. 5 presents an example of such a trajectory. The reference reel out speed v_t^{ref} for the winch is computed by a proportional force-tracking controller that exploits the measure of the tether force magnitude at the ground station:

$$v_t^{ref} = -K_{winch}(F_{ref} - \|\boldsymbol{F}_{t_{GS}}\|_2)$$

where K_{winch} is the controller gain.
To describe the flight controller, we consider an auxiliary, inertial coordinate frame $B = (L, M, N)$, named traction frame, see Fig. 5. In the remainder, the upper script B will be used to indicate that a vector is expressed in such a frame. Frame B is defined by choosing the following design parameters, which are typical in AWES: the minimum tether length during the traction phase, $\ell_{t,min}$, the

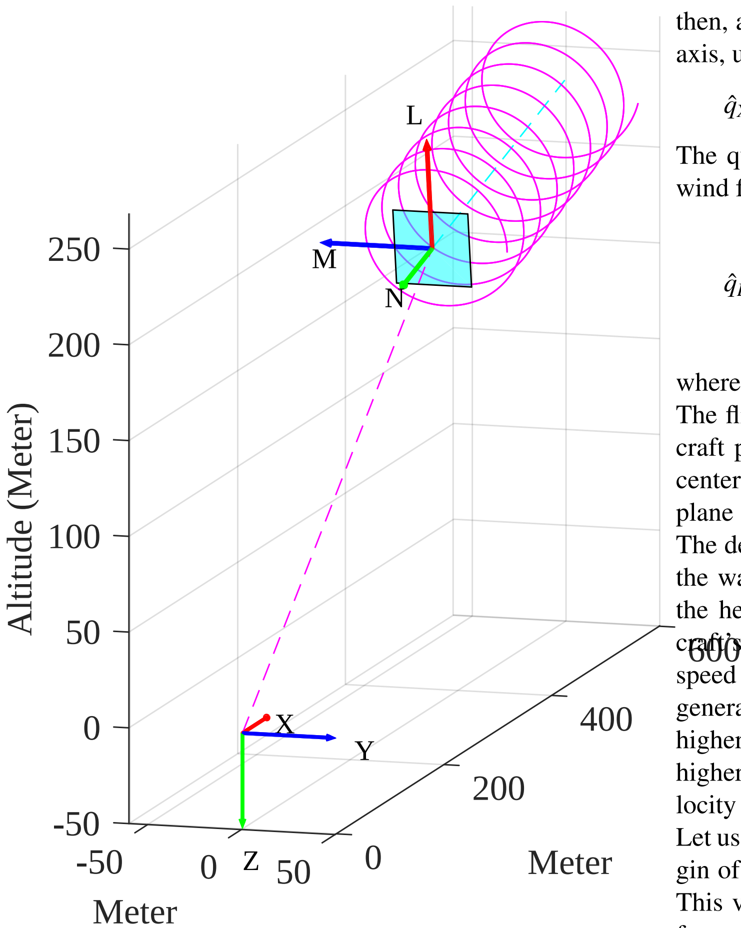

Fig. 5. Example of the targeted flight trajectory, showing the traction phase coordinate systems $A = (X,Y,Z)$ and $B = (L,M,N)$.

minimum flight altitude, h_{min}, the radius of the desired helical pattern, R_t, finally the inclination of the helix axis relative to the Earth's surface, θ_h. Based on these parameters, the vector $\boldsymbol{O}_B$ pointing from the origin of frame A to the origin of B, expressed in frame A, is obtained as:

$$\boldsymbol{O}_B = \begin{bmatrix} O_{B,x} \\ O_{B,y} \\ O_{B,z} \end{bmatrix} = \begin{bmatrix} \sqrt{{\ell_{t,min}}^2 + (h_{min} + R_t \cos(\theta_h))^2} \\ 0 \\ -(h_{min} + R_t \cos(\theta_h)) \end{bmatrix} \tag{11}$$

Vector $\boldsymbol{O}_B$ is shown with the dashed magenta line in Fig. 5. Basically, the traction frame can be obtained by applying a translation and a rotation to the coordinate axes of the wind frame A. The translation is described in (11), while the rotation is obtained by applying first a right-hand rotation with amplitude $\theta_h + \pi$ about the Y-axis, with the quaternion

$$\hat{q}_Y = [\cos((\theta_h + \pi)/2)\ \ 0\ \ \sin((\theta_h + \pi)/2)\ \ 0]^T.$$

then, a right-hand rotation with amplitude π about the X-axis, using the quaternion

$$\hat{q}_X = [\cos(\pi/2)\ \ \sin(\pi/2)\ \ 0\ \ 0]^T.$$

The quaternion $\hat{q}_{B/A}$ that performs the rotation from the wind frame to the traction frame is thus:

$$\hat{q}_{B/A} = \begin{bmatrix} q_{0_{B/A}} \\ q_{1_{B/A}} \\ q_{2_{B/A}} \\ q_{3_{B/A}} \end{bmatrix} = \hat{q}_Y * \hat{q}_X$$

where $*$ denotes the quaternion multiplication.
The flight controller shall make the projection of the aircraft position on the (L,M)-plane follow a circular path centered at the origin of frame B. For clarity, the (L,M)-plane is shown as a transparent cyan rectangle in Fig. 5. The desired circular path corresponds to the projection of the wanted helical pattern on plane (L,M). The pitch of the helix will be non-constant as it depends on the aircraft's velocity vector, which in turn depends on the wind speed and reference force set for the winch controller. In general, the larger the wind speed seen by the aircraft, the higher will be all three components of its velocity, while a higher reference force F_{ref} will lead to higher (L,M) velocity components and lower N component.
Let us now consider the aircraft position relative to the origin of the traction frame and expressed in the latter, $\boldsymbol{p}^B_{O_B}$. This vector can be computed using the coordinate transformation rules for quaternions and considering the aircraft position in wind frame, $\boldsymbol{p}_k$, and vector $\boldsymbol{O}_B$:

$$\begin{bmatrix} 0 \\ \boldsymbol{p}^B_{O_B} \end{bmatrix} = \begin{bmatrix} 0 \\ p^B_{O_B,L} \\ p^B_{O_B,M} \\ p^B_{O_B,N} \end{bmatrix} = \hat{q}^{-1}_{B/A} * \begin{bmatrix} 0 \\ \boldsymbol{p}_k - \boldsymbol{O}_B \end{bmatrix} * \hat{q}_{B/A}$$

In a similar way, the velocity vector of the aircraft in the wind frame $\dot{\boldsymbol{p}}_k$ is transformed to the traction frame as (considering that both reference frames A and B are fixed):

$$\begin{bmatrix} 0 \\ \dot{\boldsymbol{p}}_k{}^B \end{bmatrix} = \begin{bmatrix} 0 \\ \dot{p}^B_L \\ \dot{p}^B_M \\ \dot{p}^B_N \end{bmatrix} = \hat{q}^{-1}_{B/A} * \begin{bmatrix} 0 \\ \dot{\boldsymbol{p}}_k \end{bmatrix} * \hat{q}_{B/A}$$

Now, the distance d of the aircraft from the origin of the traction frame B is:

$$d = \left\| \begin{bmatrix} p^B_{O_B,L} \\ p^B_{O_B,M} \end{bmatrix} \right\|_2$$

In order to follow the desired circular path, the so-called vector field orbit guidance algorithm from [15] is used. This approach entails calculating the aircraft's desired course in the traction frame, denoted by χ^c:

$$\chi^c = \arctan\left(\frac{p^B_{O_B,M}}{p^B_{O_B,L}}\right) + \pi/2 + \arctan(K_c(d - R_t)/R_t)$$

where the gain K_c affects how aggressively the path error corrections are made. The velocity angle of the aircraft projected in the (L,M)-plane υ is given by:

$$\upsilon = \arctan\left(\frac{\dot{p}_M^B}{\dot{p}_L^B}\right)$$

and the reference yaw rate r_{ref} about the N-axis is then calculated as:

$$r_{ref} = K_\upsilon(\chi^c - \upsilon) \tag{12}$$

with the proportional gain K_υ being a design parameter.
The computed reference yaw rate (12) can be tracked, in general, by using either the rudder or the aileron, or a combination of both, see also [19]. In fact, as a first approximation, one can assume that the body z-axis is aligned with the N-axis during looping, and that the x-axis is aligned with the aircraft's velocity vector. Thus, the yaw moment induced by a rudder deflection would directly translate into a yaw rate about the N-axis, while an aileron deflection would produce a centripetal force component, which induces a turning maneuver with angular velocity aligned with the N-axis as well. Using the ailerons allows one to obtain tighter paths, however at the cost of lower force pulling the tether, since a larger part of the aerodynamic lift is employed to counteract the centrifugal force. For this reason, in the proposed control strategy the desired yaw rate is tracked by means of the rudder only, while the aileron deflection δ_a is set to zero. The rudder deflection δ_r is computed by a lower-level proportional controller:

$$\delta_r = K_r(r_{ref} - r)$$

where K_r is chosen by the designer. Regarding the pitch motion, a fixed elevator deflection in the traction phase $\delta_{e,t}$ is used, and its value is chosen to increase the angle of attack in order to have higher tether tension. Such a choice is an established practice in Kitemill and finds its theoretical justification in the flight stability analysis of rigid, single-tethered aircrafts, presented in [20]. This study shows that, in tethered flight, the aircraft pitch dynamic has an equilibrium with a dominant eigenmode, named "Loyd mode". Convergence of this mode is mainly affected by the tether attachment point on the aircraft. In other words, with a suitable choice of the tether attachment position relative to CG, the aircraft's pitch can be passively stabilized, and there is no need of active pitch control. In our simulated system, attaching the tether to the CG complies with such a stability condition. Therefore, a fixed elevator deflection in the traction phase, $\delta_{e,t}$, is used, and its value is an additional degree of freedom to adjust the tether force, if needed.
About the controller's tuning, the gains K_υ and K_r can be tuned via classical cascade control design techniques, considering a linearized model of the aircraft's attitude dynamics and imposing suitable close-loop bandwidth values. Then, using the traction phase simulator, the gain K_c can be tuned, by keeping the chosen values of the other gains constant, starting from a small value and increasing it until the flight trajectory becomes close to the wanted helical path.

3.2. Fault detection

In [14], the fault-tolerant approach employed a daisy chain allocation strategy between discrete surfaces and propellers, which could engage the latter also in non-faulty conditions. Here, the daisy chain approach has been removed for two reasons: first, the apparent airspeed of the aircraft in the traction phase is high enough to provide sufficient control authority by using only the discrete surfaces, second, using the rotors leads to higher onboard energy consumption. Thus, during the traction phase, the rotors shall not be used in non-faulty conditions. However, they can still be exploited to retain control authority in case of a fault of the rudder, allowing the aircraft to continue flying in crosswind until reaching a suitable attitude to terminate the traction phase without risking a stall or entangling with the tether.
The architecture of the proposed AFTC scheme is shown in Fig. 6. First, the desired moment $\boldsymbol{M}_d$ generated by the discrete surfaces' deflection is estimated as follows:

$$\begin{aligned}\boldsymbol{M}_d &= \begin{bmatrix} M_{x,d} \\ M_{y,d} \\ M_{z,d} \end{bmatrix} \\ &= \underbrace{\begin{bmatrix} q_\infty SbC_{l,a} & 0 & q_\infty SbC_{l,r} \\ 0 & q_\infty S\bar{c}C_{m,e} & 0 \\ q_\infty SbC_{n,a} & 0 & q_\infty SbC_{n,r} \end{bmatrix}}_{\hat{B}_S^{-1}} \begin{bmatrix} \delta_a \\ \delta_e \\ \delta_r \end{bmatrix}\end{aligned} \tag{13}$$

where $\hat{B}_S$ is the dynamic control effectiveness matrix, which is updated online based on the aircraft's relative airspeed and its aerodynamic characteristics. In particular, $C_{l,a}$ is the coefficient of incremental roll moment due to aileron deflection, $C_{l,r}$ is the coefficient of incremental roll moment due to rudder deflection, $C_{m,e}$ is the coefficient of incremental pitching moment due to elevator deflection, $C_{n,a}$ is the coefficient of incremental yaw moment due to aileron deflection, and $C_{n,r}$ is the coefficient of incremental yaw moment due to rudder deflection. These coefficients are specific to the considered aircraft and can be extracted from its aerodynamic tables; we used those presented in [16] for the simulation tests in this paper. Then, for the sake of fault detection, we consider the angular accelerations of the aircraft in the body frame, and compute the following residuals regarding the longitudinal and vertical axes:

$$\begin{aligned} R_x &= (c_1 r + c_2 p)q + c_3 M_{x,d} + c_4 M_{z,d} - \hat{\dot{p}} \\ R_y &= c_5 PR - c_6(p^2 - r^2) + c_7 M_{y,d} - \hat{\dot{q}} \\ R_z &= (c_8 p + c_2 r)q + c_4 M_{x,d} + c_9 M_{z,d} - \hat{\dot{r}} \end{aligned}$$

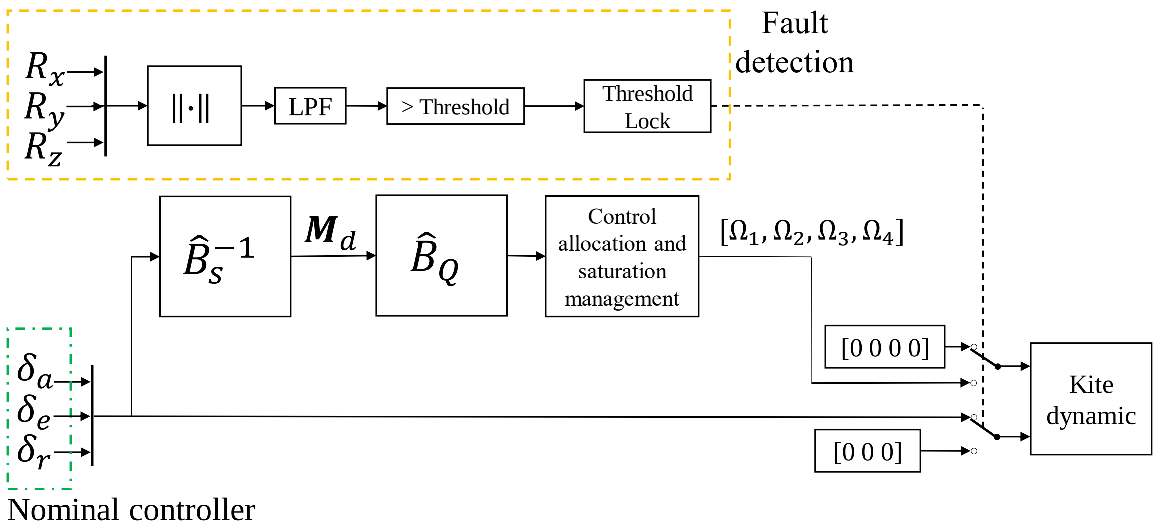

Fig. 6. Active Fault-Tolerant Control structure for the considered hybrid fixed-wing quad-rotor.

where $\hat{p}$,$\hat{q}$ and $\hat{r}$ are the estimated angular accelerations around the aircraft x, y and z axes, respectively, obtained by numerical differentiation of the measured roll and yaw rate and applying appropriate low pass filters to suppress unwanted high-frequency noise. The 2-norm of the residuals R_x,R_y, and R_z, denoted with R_{2-norm}, is used for failure detection. During looping, the R_{2-norm} signal contains high-frequency components in normal (i.e., non-faulty) conditions due to tether force oscillations. To suppress such components, which are not linked to faults, a low-pass filter (LPF in Fig. 6) is employed, tuned on the basis of data collected in non-faulty system operation. In particular, we used a first-order filter with bandwidth equal to 3.4 rad/s, discretized at 0.01 s, which is also the control sampling period. The absolute values of the filtered residuals are then used to detect a fault in the actuation system by setting a suitable threshold. Once the failure indicator is triggered, a threshold lock algorithm is used to hold this condition even if the residuals fall below the threshold, and the actuation system is reconfigured to employ the four rotors instead of the rudder, as described next.

3.3. Quad rotor control allocation and saturation management

After detecting the fault, all the discrete surface commands are set to zero, and the desired moment is allocated to the rotors as follows:

$$\begin{bmatrix} \Omega_1^2 \\ \Omega_2^2 \\ \Omega_3^2 \\ \Omega_4^2 \end{bmatrix} = \hat{B}_Q \begin{bmatrix} F_{T_{z,d}} \\ \boldsymbol{M}_d \end{bmatrix} \tag{14}$$

where $F_{T_{z,d}}$ is a user-chosen total thrust force, and $\hat{B}_Q$ is the control allocation matrix, computed as:

$$\hat{B}_Q = \begin{bmatrix} b_1 & b_2 & b_3 & b_4 \\ -b_1 x_p & b_2 x_p & b_3 x_p & -b_4 x_p \\ b_1 y_p & -b_2 y_p & b_3 y_p & -b_4 y_p \\ c_1 & c_2 & c_3 & c_4 \end{bmatrix}^{-1} \tag{15}$$

The terms b_i and c_i, $i = 1, \dots, 4$ in (15) are time-varying and computed as:

$$b_i = T_{i,max}/\Omega_{M,max}^2$$

$$c_i = Q_{i,max}/\Omega_{M,max}^2$$

where $T_{i,max}$ and $Q_{i,max}$ are, respectively, the maximum thrust and torque achievable by propeller i based on the current state of the plant, obtained using the derived rotors' look-up tables (see equations (2)-(5)), and $\Omega_{M,max}$ is the motor's maximum speed. Regarding the choice of $F_{T_{z,d}}$ in (14), in untethered quad-copter control this would be normally set on the basis of the vertical motion of the drone, for example using a vertical position or speed controller. However, in tethered flight during the traction phase, this value can be set to zero since the lift force produced by the rigid wing is large enough.
Applying (14), it can happen that some of the Ω_i values are out of range, i.e. higher than $\Omega_{M,max}$ or lower than a minimum value $\Omega_{M,min}$, set by the user (typically about 20% of the maximum speed in this application). In these cases, to avoid an uncontrolled alteration of the applied moments, we propose a rotor saturation management algorithm, presented in Fig. 7. Essentially, the algorithm considers the three possible cases of rotor speed saturation:

1. If any allocated speed is below $\Omega_{M,min}$ and none exceeds $\Omega_{M,max}$, then all rotors' speeds are increased by a factor K_u which is large enough to avoid the lower speed limit, maintaining the equivalent moment effect. The increase in rotors' speed will lead to a larger total thrust, which is typically much smaller than the aerodynamic lift force during crosswind flight and will be eventually compensated by the ground station controller to keep the same tether force. Specifically, the gain is

$$K_u = \frac{\Omega^2_{M,max} - \hat{B}_Q^{(i_{max},1)} F_{T_{z,d}}}{\hat{B}_Q^{(i_{max},2)} M_{d,x} + \hat{B}_Q^{(i_{max},3)} M_{d,y} + \hat{B}_Q^{(i_{max},4)} M_{d,z}} \quad (16)$$

where $\hat{B}_Q^{(i,j)}$ indicates the element in the i^{th} row and j^{th} column of matrix $\hat{B}_Q$, and i_{max} is the index of the rotor with largest speed;

2. If any speed value is above $\Omega_{M,max}$ and none is below $\Omega_{M,min}$, then all rotors spinning speeds are scaled down by the factor K_d:

$$K_d = \frac{\Omega^2_{M,min} - \hat{B}_Q^{(i_{min},1)} F_{T_{z,d}}}{\hat{B}_Q^{(i_{min},2)} M_{d,x} + \hat{B}_Q^{(i_{min},3)} M_{d,y} + \hat{B}_Q^{(i_{min},4)} M_{d,z}}$$

where i_{min} is the index of the rotor with the smallest speed. If, afterwards, any rotor speed is below $\Omega_{M,min}$, then all values are scaled up by the factor K_u following equation (16).

3. If both upper and lower limits are violated, then the algorithm calculates which limit is exceeded the most and applies the corresponding procedure of either case 1) or 2).

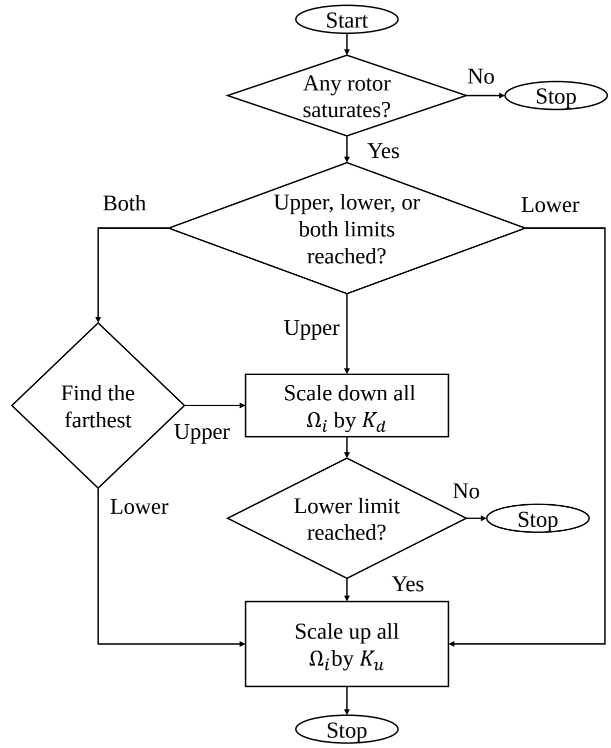

Fig. 7. Rotor speeds' saturation management

4. SIMULATION RESULTS

4.1. Model and control parameters

The parameters of the AWES model and control system considered in our simulations are reported in Tables 1-3. Regarding the aircraft, all aerodynamic data, dimensions, mass, and inertia matrix for the considered system have been taken from [16]; for the sake of space, we refer the reader to this source for details and the numerical values. To carry out the simulations, we employed Matlab and Simulink with a variable step solver, in particular `ode45` with relative tolerance equal to 10^{-3}. The control and fault detection/recovery algorithms have been implemented in discrete time with a sampling period of 0.01 s.

4.2. AFTC simulation

To test the proposed AFTC approach, we carried out extensive simulations with average wind speed in the range 8-14 m/s, a uniformly distributed wind perturbation along all three axes in the range ±10% of the average value, and random injection of a rudder failure at different points during the looping maneuver. In all the tested cases, the approach successfully identified the fault and reconfigured the actuation system to safely continue system operation. As an example, we describe here the results obtained with 12 m/s average wind speed and fault injection when the aircraft is at the bottom of the loop. Three scenarios are presented: a no-failure scenario, a rudder failure scenario without AFTC, and a rudder failure scenario with AFTC. The rudder failure has been injected in the simulator at 35 s, such that the rudder is stuck at zero degrees. Fig. 8 shows the rudder deflection in the three scenarios. In Fig. 9, the aircraft trajectory in the no-failure scenario is compared with the one in the rudder failure scenario without applying the proposed AFTC method. The figure shows that in the latter case, the aircraft does not maintain an

Table 1. Ground station and aircraft parameters

Parameter and symbol	Value	Unit
Aircraft mass m_a	4.778	kg
Aircraft inertia $J_{xx,yy,zz,xz}$	1.74, 0.28, 1.83, -0.02	kg m^2
Aircraft wing area S	0.76	m^2
Aircraft wingspan b	3.7	m
Aircraft mean chord $\bar{c}$	0.22	m
Winch time constant τ_w	0.16	s

Table 2. Rotors/Propellers' parameters

Parameter and symbol	Value	Unit
Zero lift drag coefficient of the propeller blade airfoil C_{d_0}	0.03	-
Rotor moment of inertia about spin axis J_P	$1.2201\ 10^{-4}$	$\mathrm{kg\,m^2}$
Propeller radius R_p	0.3841	m
Number of blades in each propeller b_p	2	-
Propeller blade effective chord c_p	0.0823	m
Propeller root blade angle θ_0	12.3056	deg
Propeller linear twist along the blade θ_1	-4.6146	deg
Propeller airfoil lift curve slope a_p	4	-
Rotors maximum spinning speed $\Omega_{M,max}$	5000	rpm
Rotors minimum spinning speed $\Omega_{M,min}$	1000	rpm

Table 3. Controllers' parameters

Parameter and symbol	Value	Unit
Reference tether force on the winch F_{winch}	700	N
Winch speed controller gain K_{winch}	0.03	-
Circular path controller gain K_c	0.6	-
Yaw rate controller gain K_υ	1.5	-
Rudder controller gain K_r	-0.6	-
Elevator deflection in traction phase $\delta_{e,T}$	-5	deg
Desired total thrust force for rotors' allocation $F_{T_{z,d}}$	0	N

acceptable flying trajectory. In a real flight, this may lead to unpredictable situations, including structural damage if the aircraft is entangled by the tether, or a stall. The simulator shows that the aircraft starts to fly in smaller circles after the failure is injected. The divergence from the desired path in case of discrete surface failure can take less than one loop to be severe, this can be observed from the

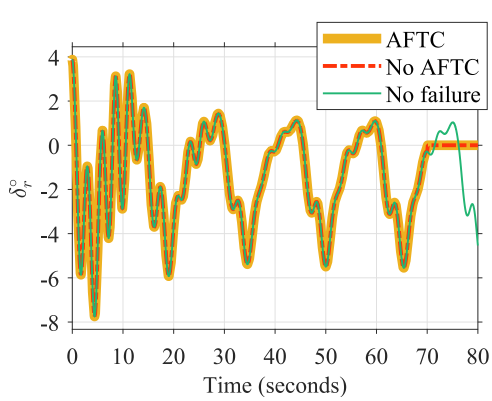

Fig. 8. Rudder surface deflection δ_r° in the three scenarios.

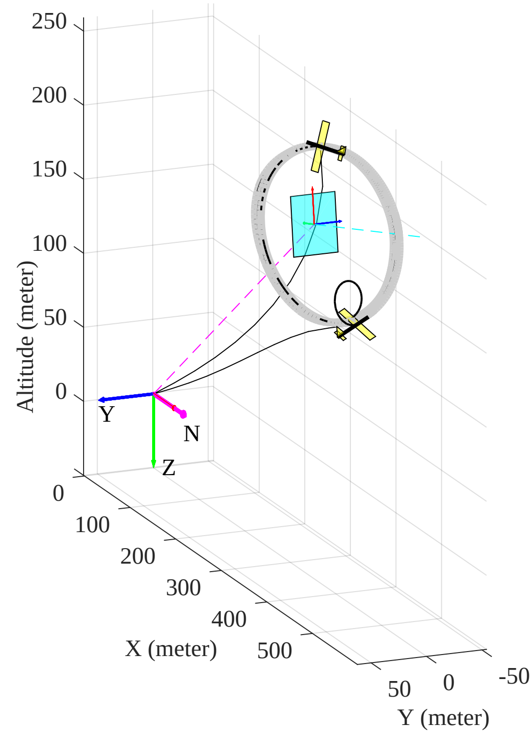

Fig. 9. Aircraft trajectory in the simulator in the no-failure scenario (thick gray line), and in the rudder failure scenario without applying AFTC (black thin line).

aircraft altitude which is illustrated for the three scenarios in Fig. 10.

In the third scenario, the AFTC method is applied. The residuals are exploited to detect the failure, the R_{2-norm} threshold is set to 10 (rad/s^2). Fig. 11 presents the residuals' R_{2-norm} in the three scenarios. With our AFTC approach, the rotors are used to recover from the fault. The resulting trajectory is compared with the non-faulty one in Fig. 12, and the moments exerted on the aircraft body with the AFTC approach are shown in Fig. 13. It can be noted that in this case, the aircraft is able to maintain an acceptable path notwithstanding the rudder fault.

In Figs. 14-15 we present the results obtained when the

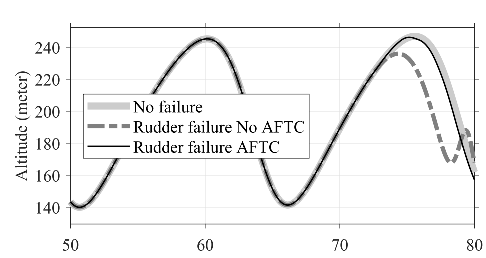

Fig. 10. Comparison of the aircraft altitude in the three scenarios.

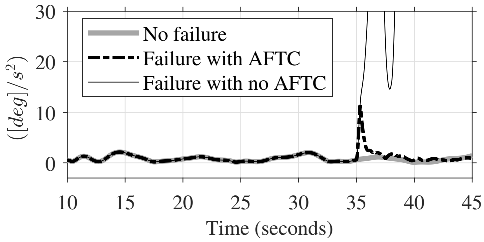

Fig. 11. Comparing the residuals' R_{2-norm} in the three scenarios.

fault is injected at four representative points: on top of the loop, at the bottom, and on each side (i.e. one ascending, and one descending). It can be noted that in all cases, the AFTC allows the aircraft to continue its flight with very little discrepancy with respect to the non-faulty scenario (Fig. 15), while without AFTC the flight trajectory is always compromised, see Fig. 14. Finally, Figs. 16-17 report a quantitative analysis of the discrepancy between the flight trajectory with and without AFTC. In fact, they present the average and maximum values of the Euclidean distance $\|\tilde{\boldsymbol{p}}_k(t) - \bar{\boldsymbol{p}}_k(t)\|_2$ where $\bar{\boldsymbol{p}}_k(t)$ is the aircraft position without any fault, and $\tilde{\boldsymbol{p}}_k(t)$ the position with a rudder fault and either no countermeasure (Fig. 16) or the proposed AFTC (Fig. 17). The average and maximum values are computed over a tim period corresponding to one full loop in the non-faulty scenario, starting from when the fault occurs. It can be noted that the AFTC keeps the average and worst-case distance among trajectories at very low values, in the order of 5 m, while the discrepancy without any fault tolerant approach is one order of magnitude larger, i.e. about 50 m on average and more than 150 m maximum in the considered time span.

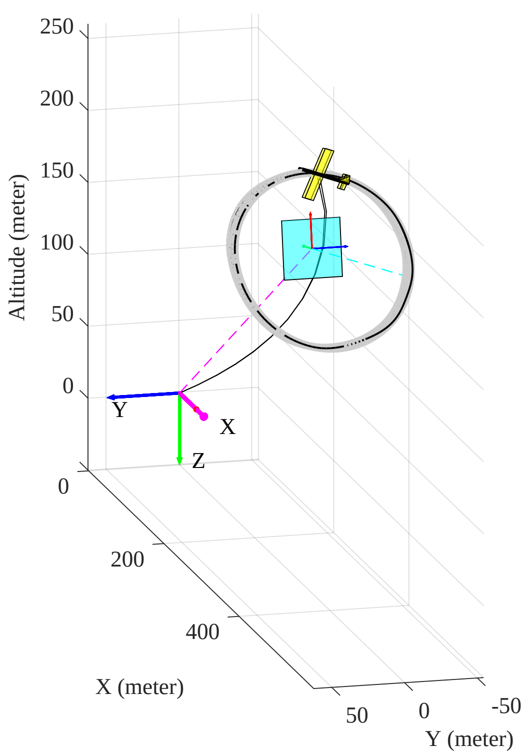

Fig. 12. Aircraft trajectory in the no-failure scenario (thick gray line), and in the rudder failure scenario with the proposed AFTC approach (thin black line).

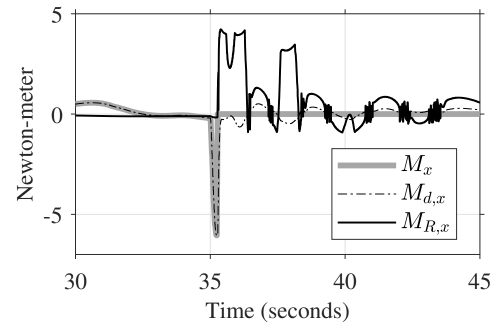

(a) Moments about X-body axis

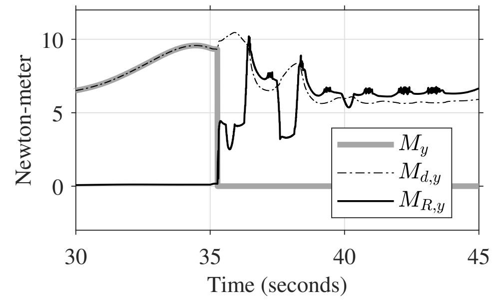

(b) Moments about Y-body axis

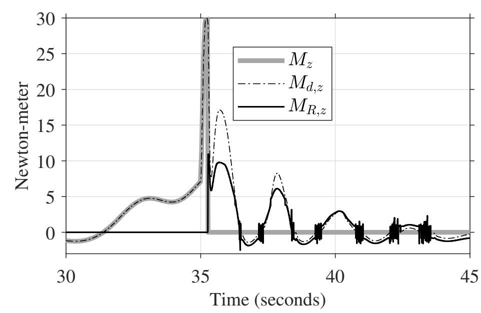

(c) Moments about Z-body axis

Fig. 13. Simulation of the faulty scenario with AFTC. Moments applied by the surfaces, desired moments, and moments applied by the rotors about the aircraft body axes.

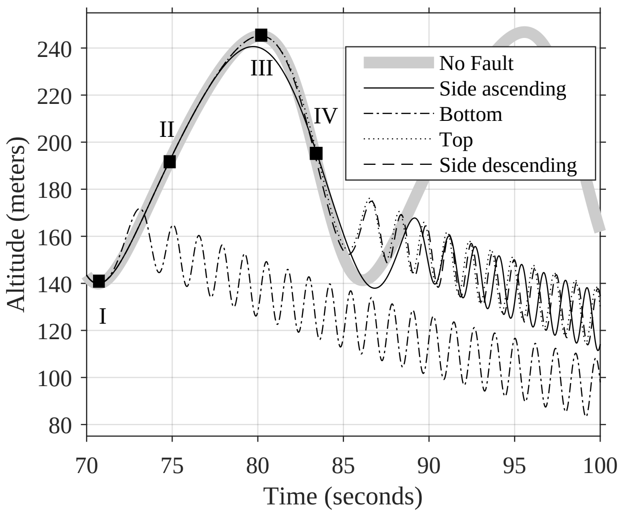

Fig. 14. Aircraft altitude in the non-faulty scenario (thick gray line) and in presence of a rudder fault injected at the bottom of the loop (I), in the ascending part (II), at the top (III), and in the descending part (IV), without any fault detection and recovery approach.

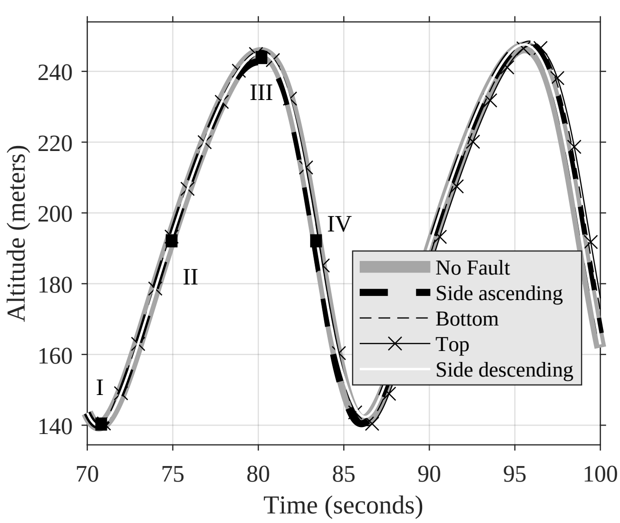

Fig. 15. Aircraft altitude in the non-faulty scenario (thick gray line) and in presence of a rudder fault injected at the bottom of the loop (I), in the ascending part (II), at the top (III), and in the descending part (IV), with the proposed AFTC approach.

5. CONCLUSIONS AND FUTURE DEVELOPMENTS

A new active fault-tolerant control (AFTC) approach for the traction phase of a pumping airborne wind energy system using a hybrid fixed-wing/quad-rotor aircraft has been presented and tested in simulation. As seen from the simulation results, the suggested AFTC is able to maintain acceptable performance in the presence of sudden discrete control surface failures. Possible future developments of this research are the development of approaches for other fault scenarios, for example during other operational phases, and of an overall fault management approach able to bring the system to a safe state, eventually landing the aircraft on the ground platform.

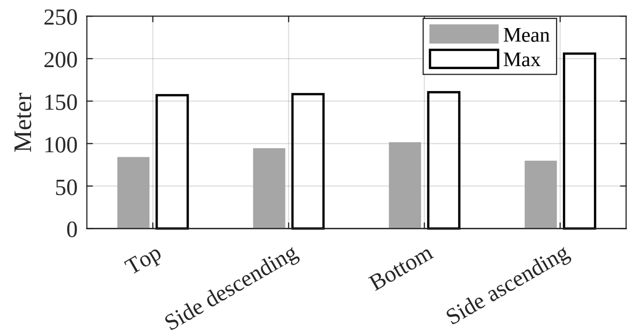

Fig. 16. Average and maximum distance between the aircraft trajectory in the non-faulty scenario and the one obtained with a rudder fault injected at four representative points in a loop, without any fault detection and recovery approach. The average and maximum values are computed over a time period corresponding to one loop in the non-faulty case.

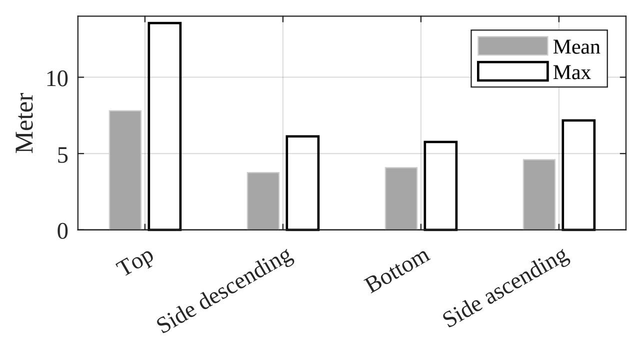

Fig. 17. Average and maximum distance between the aircraft trajectory in the non-faulty scenario and the one obtained with a rudder fault injected at four representative points in a loop, with the proposed AFTC approach. The average and maximum values are computed over a time period corresponding to one loop in the non-faulty case.

DECLARATIONS

Funding and/or Conflicts of interests/Competing interests. The authors declare that they have no known competing financial interests or personal relationships that could have appeared to influence the work reported in this paper.

REFERENCES

[1] Cristina L. Archer and Ken Caldeira. Global assessment of high-altitude wind power. *Energies*, 2(2):307–319, 2009.

[2] Cristina L. Archer, Luca Delle Monache, and Daran L. Rife. Airborne wind energy: Optimal locations and variability. *Renewable Energy*, 64:180–186, 2014.

[3] Florian Bauer and Ralph M. Kennel. Fault-tolerant power electronic system for drag power kites. *Journal of Renewable Energy*, 2018:1306750, Apr 2018.

[4] Philip Bechtle et al. Airborne wind energy resource analysis. *Renewable Energy*, 141:1103–1116, Oct 2019.

[5] Andrea Berra and Lorenzo Fagiano. An optimal reeling control strategy for pumping airborne wind energy systems without wind speed feedback. In *2021 European Control Conference (ECC)*, pages 1199–1204, 2021.

[6] M. Bolognini and L. Fagiano. Lidar-based navigation of tethered drone formations in an unknown environment. *IFAC-PapersOnLine*, 53(2):9426–9431, 2020. 21st IFAC World Congress.

[7] BVG Associates. Getting airborne – the need to realise the benefits of airborne wind energy for net zero, available at https://airbornewindeurope.org. 2022.

[8] Antonello Cherubini et al. Airborne Wind Energy Systems: A review of the technologies. *Renewable Sustainable Energy Rev.*, 51:1461–1476, Nov 2015.

[9] Hisham Eldeeb. *Modelling, Control and Post-Fault Operation of Dual Three-phase Drives for Airborne Wind Energy*. Dissertation, Technische Universität München, 2019.

[10] L. Fagiano, M. Milanese, and D. Piga. High-altitude wind power generation. *IEEE Transactions on Energy Conversion*, 25(1):168 –180, mar. 2010.

[11] L. Fagiano and S. Schnez. On the take-off of airborne wind energy systems based on rigid wings. *Renewable Energy*, 107:473–488, 2017.

[12] Lorenzo Fagiano, Manfred Quack, Florian Bauer, Lode Carnel, and Espen Oland. Autonomous airborne wind energy systems: Accomplishments and challenges. *Annual Review of Control, Robotics, and Autonomous Systems*, 5(1), 2022.

[13] H. T. K. Linskens et al. Tether Dynamics Analysis and Guidance and Control Design for Active Space-Debris Removal. *Journal of Guidance, Control, and Dynamics*, Mar 2016.

[14] Tareg Mohammed and Lorenzo Fagiano. Fault- tolerant control of a tethered aircraft for airborne wind energy. In *2022 IEEE Conference on Control Technology and Applications (CCTA)*, pages 279–284, 2022.

[15] Derek R. Nelson, D. Blake Barber, Timothy W. McLain, and Randal W. Beard. Vector field path following for miniature air vehicles. *IEEE Transactions on Robotics*, 23(3):519–529, 2007.

[16] Sebastian Rapp et al. Cascaded Pumping Cycle Control for Rigid Wing Airborne Wind Energy Systems. *Journal of Guidance, Control, and Dynamics*, 42(11):1–18, Jun 2019.

[17] Volkan Salma et al. Improving reliability and safety of airborne wind energy systems. *Wind Energy*, 23(2):340–356, Feb 2020.

[18] Brian L. Stevens et al. *Aircraft Control and Simulation: Dynamics, Controls Design, and Autonomous Systems, 3rd Edition*. Wiley, Nov 2015.

[19] Davide Todeschini, Lorenzo Fagiano, Claudio Micheli, and Aldo Cattano. Control of a rigid wing pumping airborne wind energy system in all operational phases. *Control Engineering Practice*, 111:104794, 2021.

[20] Filippo Trevisi, Alessandro Croce, and Carlo E. D. Riboldi. Flight stability of rigid wing airborne wind energy systems. *Energies*, 14(22), 2021.

[21] O Tulloch, A Kazemi Amiri, H Yue, J Feuchtwang, and R Read. Tensile rotary power transmission model development for airborne wind energy systems. *Journal of Physics: Conference Series*, 1618(3):032001, sep 2020.

[22] Karel van Hussen, Enno Dietrich, Job Smeltink, Koen Berentsen, Manel van der Sleen, Robert Haffner, and Lorenzo Fagiano. *Study on challenges in the commercialisation of airborne wind energy systems*. European Commission and Directorate-General for Research and Innovation, Publications Office, 2018.

Tareg Mohammed received the M.Sc. in electrical engineering, control engineering and intelligent systems from Bandung Institute of Technology, Bandung, Indonesia, in 2017, and the B.Sc. in aeronautical engineering (avionics) from Sudan University of Science and Technology, Khartoum, Sudan, in 2008. In 2019 he started his Ph.D. research at Politecnico di Milano. In 2021 he started to work in AWES company (Kitemill AS) as a control system engineer. His current research interests include airborne wind energy simulation and control, and Fault-tolerant control for AWES.

Espen Oland received the Ph.D. degree in engineering cybernetics from the Norwegian University of Science and Technology in 2014. From 2008 to 2010, he was an Assistant Professor with NUC. In 2012, he was a Visiting Research Scholar with The Ohio State University, Columbus, Ohio, under the supervision of A. Serrani. The last decade he has worked as a researcher at Teknova focusing on condition based maintenance, and as a Product Development Manager at Kitemill AS developing airborne wind energy systems. Oland is currently employed as a senior project engineer at Kongsberg Defence and Aerospace, and holds an associate professor position at UiT - The Arctic University of Norway. His current research interests include the control of unmanned aerial vehicles, airborne wind energy systems, spacecraft, underactuated rigid bodies, and behavioral control methods.

Lorenzo Fagiano received the Ph.D. degree in information and systems engineering from the Politecnico di Torino, Torino, Italy, in 2009. He is currently Full Professor of automation and control engineering at the Politecnico di Milano. His research interests include constrained estimation and control, set membership methods, and applications to industrial, robotic, and energy systems. He is the recipient of the 2019 European Control Award, the Mission Innovation Champion Award 2019 for Italy, and the 2010 ENI Award Debut in Research Prize.